

Preliminary Design and Evaluation of an Airfoil with Active Continuous Trailing-Edge Flap

Jinwei Shen¹, Robert P. Thornburgh², Andrew R. Kreshock², Matthew L. Wilbur², and Yi Liu¹

¹National Institute of Aerospace, Hampton, VA 23666

²Army Research Laboratory, Vehicle Technology Directorate, Hampton, VA 23681

Abstract

This paper presents the preliminary design and evaluation of an airfoil with an active continuous trailing-edge flap (CTEF) as a potential rotorcraft active control device. The development of structural cross-section models of a continuous trailing-edge flap airfoil is described. The CTEF deformations with MFC actuation are predicted by NASTRAN and UM/VABS analyses. Good agreement is shown between the predictions from the two analyses. Approximately two degrees of CTEF deflection, defined as the rotation angle of the trailing edge, is achieved with the baseline MFC-PZT bender. The 2D aerodynamic characteristics of the continuous trailing-edge flap are evaluated using a CFD analysis. The aerodynamic efficiency of a continuous trailing-edge flap is compared to that of a conventional discrete trailing-edge flap (DTEF). It is found that the aerodynamic characteristics of a CTEF are equivalent to those of a conventional DTEF with the same deflection angle but with a smaller flap chord. A fluid structure interaction procedure is implemented to predict the deflection of the continuous trailing-edge flap under aerodynamic pressure. The reductions in CTEF deflection are minimal when aerodynamic pressure is applied: 2.6% reduction is shown with a CTEF deflection angle of two degrees and at angle of attack of six degrees. In addition, newly developed MFC-PMN actuator is found to be a good supplement to MFC-PZT when applied as the bender outer layers. A mixed MFC-PZT and MFC-PMN bender generates 8% more CTEF deflection than an MFC-PZT or an MFC-PMN only bender under aerodynamic loads.

Nomenclature

c	Chord
C_d	Section drag coefficient
C_l	Section lift coefficient
C_m	Section moment coefficient
C_p	Section pressure coefficient
d_{33}	Piezoelectric strain constant

PMN	Lead magnesium niobate
PZT	Lead zirconate titanate

Acronym

AOA	Angle of attack
ATE	Active trailing edge
ATR	Active twist rotor
CFD	Computational fluid dynamics
CTEF	Continuous trailing-edge flap
DTEF	Discrete trailing-edge flap
FSI	Fluid structure interaction
MFC	Macro fiber composite

Introduction

The helicopter has suffered high vibration and noise levels since its inception. These are inherent to the design and is caused primarily by long flexible rotor blades rapidly rotating in a self-induced unsteady air. If left untreated, this level of vibration and noise harms the health of passengers and shortens the life of on-board instruments and structures. Virtually all modern helicopters carry vibration reduction devices, mostly passive vibration isolators or absorbers (Ref. 1). Although these devices are effective, to a degree, in reducing vibration, active vibration and noise control systems have been widely recognized as the ultimate to achieve a jet-smooth ride (Ref. 2). Combined with other innovative low vibration and noise design techniques, helicopters with active vibration and noise control devices may eventually see larger adoption in the public transportation system.

Presented at the Future Vertical Lift Aircraft Design Conference, January 18-20, 2012 Fisherman's Wharf, San Francisco, California. Copyright © 2012 by the American Helicopter Society International, Inc. All rights reserved.

This is the reason that intense research and studies have been carried out on the subject of rotorcraft active control in recent decades. (Ref. 3).

The majority of the active control systems target the major source of the vibration and noise, the main rotor, and propose to alter its aerodynamic and dynamic behavior adaptively to achieve the control goal. Among such devices, discrete trailing-edge flaps (DTEF) received the most interest (Ref. 4). A DTEF only takes a small portion of the rotor span near the tip, but it can effectively modify the rotor response by changing the rotor pitch angle elastically. Its implementation typically consists of piezoelectric stacks as the active driving mechanism, and various hinges and levers to convert and amplify the piezoelectric strain into a DTEF deflection. The major challenge of such design is the high centrifugal loading condition found in a rotor, which is particularly challenging to DTEF systems. The brittle piezoelectric stacks tend to break, and the effectiveness of the lever amplification mechanism is reduced. An alternative to DTEF design is the Active Twist Rotor (ATR) concept (Ref. 5). Its capability in reducing vibration and noise has been shown in several wind tunnel experiments (Ref. 6). Active piezoelectric layers are built into the blade sectional layout, and the elastic twist is dynamically altered along the blade when the layers are activated. An attractive aspect of ATR lies in the unique feature of the actuators: active piezoceramic fibers are embedded in a polymeric matrix. The matrix protects the fibers, and also allows the actuators to be applied to a curved surface such as airfoil skins. A drawback of the ATR concept is that the actuators have to be applied along a major part of the blade to be effective. A modified DTEF design, Active Trailing-Edge (ATE) concept, was proposed recently (Ref. 7). In order to eliminate the aforementioned hinges and levers mechanism typically found in a DTEF, the airfoil trailing edge, which is soft in design, is deformed with a piezoceramic stack bimorph. The piezoceramic stacks used in the ATE concept, however, are still exposed to the high stress condition found in a rotor blade. In order to protect the piezostacks from breaking under adverse tension loads, the bimorph has to be cut into small patches along the spanwise direction (Ref. 8).

The current study proposes a continuous trailing-edge flap design. The CTEF design embeds planar piezoelectric layers into the airfoil layout to distort the trailing edge section dynamically instead of using piezoceramic stacks (Ref. 8). Thus it combines the advantages of the ATR and ATE concepts: eliminating moving parts typically found in a discrete trailing-edge flap such as hinges and levers and avoiding the complex arrangement of protecting piezoceramic stacks with partitioning. This simplification in structural design potentially leads to reduction in rotor weight and maintenance requirements.

The continuous trailing-edge flap is also believed to be more efficient in generating aerodynamic excitation than the discrete flap because it does not have a gap between the main airfoil and flap. Such gap leak air which results in decreased flap aerodynamic performance. The potential CTEF applications are active control of helicopter rotor vibration and noise, performance improvements, and in-flight rotor blade tracking, similar to the widely studied discrete trailing-edge flap (Ref. 9) and active twist rotor concepts (Ref. 10).

The objective of this study is to carry out a preliminary design of an airfoil with active continuous trailing-edge flap with MFC actuators, develop an analytical framework to predict active CTEF deformation with a fluid and structure interaction procedure, and evaluate the 2D aerodynamic characteristics of the CTEF by comparing to the conventional DTEF.

Analytical Model

The baseline airfoil is a NACA 0012, selected for its simplicity and its symmetry, which facilitates validations of analytical models. The design and evaluation procedure presented in this study, however, can be readily applied to modern helicopter asymmetric airfoils. The airfoil chord size is $124mm$, which was chosen as a sub-scale representation of the main rotor blade of a general utility helicopter, similar to UH-60 (Ref. 11). The sub-scale model has a scale factor of 0.234, which tested in the NASA Langley Transonic Dynamics Tunnel (TDT) with a heavy gas medium, would result in both the Mach and Froude numbers being matched to the full-scale rotor (Ref. 12). Table 1 lists some design parameters of the full and sub-scale models. All the analysis and predictions shown in this paper are for the sub-scale model. The aerodynamic pressure is calculated with the rotor tip speed in air.

Table 1: Scale parameters

Parameter		Full-scale	Sub-scale
Chord length	(mm)	531	124
Tip speed	(m/s)	221	107
Tip Mach number	(Air)	0.65	0.31
Tip Reynolds number	(Air)	8e+6	0.9e+6

Multidisciplinary analyses are required to calculate the aeroelastic deformation of an airfoil with active continuous trailing-edge flaps. The structural analyses implemented to predict the 2D deformation of continuous trailing-edge flap section are MSC/NASTRAN (Ref. 13), an industry-standard FEM analysis, and UM/VABS (Variational-Asymptotic Beam Cross-Sectional)

developed at the University of Michigan (Ref. 14). The aerodynamic analyses used to evaluate the performance of an airfoil with deformed continuous trailing-edge flap are a CFD analysis, 2D OVERTURNS (Overset Transonic Unsteady Rotor Navier-Stokes) developed at the University of Maryland (Ref. 15), and XFOIL (Ref. 16), an 2D airfoil analysis using vortex panel method. XFOIL is examined as a replacement for CFD, which is used when large numbers of calculations are required. As in the cases of parametric and optimization studies, an acceptable reduction in analysis fidelity is permitted in order to gain computation efficiency.

Structural Cross-Sectional Analyses

UM/VABS is a finite-element analysis of active cross sections based on variational-asymptotic method. It computes the cross-sectional elastic, inertial, thermal, and electric characteristics of active anisotropic beams of arbitrary sectional shape and including effects of initial twist and curvature. NASTRAN is used to validate the UM/VABS predicted deformation of an active CTEF cross-section, and is more capable in modeling complex CTEF layout with the assistance of MSC/PATRAN pre/post-processing software (Ref. 17). In the present study, thermal equivalent analysis was used in both UM/VABS and NASTRAN to capture the expansion and contraction of the actuators subjected to an applied electric field (Ref. 18) (UM/VABS, however, can model both piezoelectric actuators and sensors by solving the electro-elastic equations.) The cross-section of the CTEF airfoil is modeled with 2D shell elements in NASTRAN and solved with the linear analysis solution (SOL 101.) The same cross-section discretization mesh is used for the UM/VABS and NASTRAN models.

Figure 1 illustrates the baseline continuous trailing-edge flap layout. The baseline CTEF layout consists of a D-shaped nose spar, a bimorph piezoelectric actuator in the trailing edge, an extensible airfoil skin, and core filling materials. The “D” spar is the main load-carrying element which transfers the blade aerodynamic and inertial loads to the rotor hub. It is constructed from E-glass fabric. The baseline bimorph actuator is a rectangular-shaped bender with Macro-Fiber Composite (MFC) plies on top and bottom. Electric fields with opposite direction are applied to the top and bottom MFC layers respectively, which produce extension on the top three layers and contraction on the bottom three MFC layers. This results in a pure bending of the bimorph bender, which in turn deforms the trailing edge region. The bimorph bender connects to the “D” spar in front and ends with a secondary rib spar at the trailing edge. Besides providing actuation, the bimorph bender is the main load carrying element in the airfoil aft section, and transfers the aerodynamic and

inertial forces to the forward “D” spar. A nylon material is chosen for the airfoil skin because of its high compliance. Core filling materials are applied to maintain proper airfoil shape under aerodynamic pressure and structural loads. Rohacell foam is used inside the “D” spar and Nomex Honeycomb is used in the trailing edge region. Nomex honeycomb has smaller stiffness along the chord but larger stiffness normal to the chord. The trailing edge region filled with Nomex honeycomb is easy to bend but difficult to shear, and thus maintains proper shape under aerodynamic pressure.

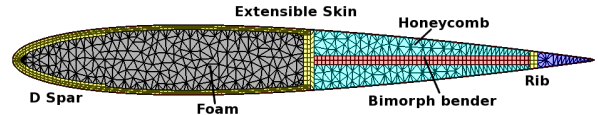


Figure 1: Baseline continuous trailing-edge flap layout.

The baseline macro-fiber composite, commonly used in the active twist rotor concept, uses PZT-5H fibers (Ref. 5). With the progress in high performance single-crystal piezoelectric materials (Ref. 19), MFCs with PMN as the active fibers have been developed (Ref. 20). MFC-PMN has been shown to have higher piezoelectric strain than MFC-PZT, however, with half the longitudinal stiffness. MFC-PMN is used as a supplement material to MFC-PZT in this study. Table 2 presents some important design parameters of the MFC bender.

Table 2: MFC bender parameters

Parameter	Value	Unit
Bender location	50% Chord	
Bender length	40% Chord	
MFC layers	3+3	
MFC layer thickness	0.3	mm
MFC-PZT d33	4.0E-10	
MFC-PZT stiffness	30.3	GPa
MFC-PMN d33	5.6E-10	
MFC-PMN stiffness	12.4	GPa
Power input	1000	V

2D Aerodynamic Analysis

The CFD code, 2D OVERTURNS, is used to compare the aerodynamic characteristics of an airfoil with deformed CTEF to the conventional discrete trailing-edge flap. The CFD code solves the compressible Reynolds-Averaged Navier-Stokes (RANS) equations with proper boundary conditions for the specified geometry on an overset structured mesh. The airfoil geometry with a deformed CTEF is obtained from the aforementioned 2D structural analyses using UM/VABS and NASTRAN.

This deformed airfoil is passed to an OVERTURNS grid generator that produces a 329×97 C-type grid using a hyperbolic mesh generation technique (Fig. 2.) The turbulence model is Spalart-Allmaras. The Mach and Reynolds number are set to the corresponding values of the sub-scale model in air (Table 1.) The DTEF is assumed to be sealed when modeled with the CFD code, and no air leaks at the flap nose. Ref 15 describes more details of the OVERTURNS CFD analysis.

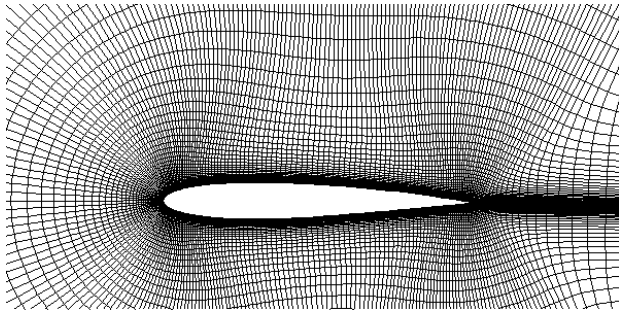


Figure 2: CFD grid of a NACA 0012 CTEF airfoil; Deformed CTEF angle = 2° .

XFOIL uses an inviscid linear-vorticity panel method with Karman-Tsien compressibility correction. The boundary layers and wake are calculated with a two-equation lagged dissipation integral method. It takes an arbitrary airfoil geometry as input, and calculates the aerodynamic coefficients and pressure distribution given Mach number, Reynolds number, and angle of attack. It can also model an airfoil with a discrete trailing-edge flap. The same CTEF airfoil geometry is used in the CFD code and the XFOIL analysis.

2D Static Fluid and Structure Interaction

The trailing edge portion of the CTEF airfoil is intentionally designed to be soft in order to deform under MFC actuation. When a CTEF is incorporated into a rotor blade rotating in air, differential aerodynamic pressures appear on the top and bottom airfoil surfaces (Fig. 3.) Although the major part of this pressure difference is located at the leading-edge due to the leading edge suction effect, the pressure difference on the trailing edge is normally not insignificant, particularly under high lift condition, such as when CTEF has a large deflection, airfoil is under high angle of attack, or airfoil is in high dynamic pressure and Mach number. The aeroelastic deformation of CTEF under such aerodynamic pressure is calculated with a Fluid and Structure Interaction (FSI) procedure.

The implementation of the FSI procedure uses a simple coupling approach. The CTEF deformation under MFC actuation is first calculated with NASTRAN for a given voltage without aerodynamic pressure loads. The

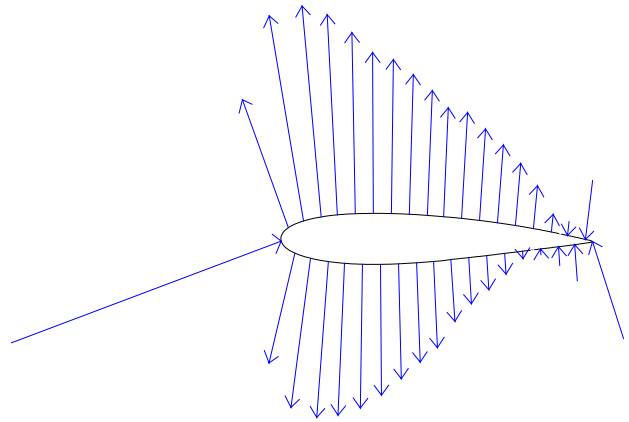


Figure 3: Aerodynamic pressure on a NACA 0012 CTEF airfoil; Deformed CTEF angle = 2° , angle of attack = 0. (Negative pressure coefficients are represented with arrow away from surface.)

deformed CTEF airfoil is passed to OVERTURNS or XFOIL, and aerodynamic pressure is obtained for a given operation condition (fluid properties, angle of attack, Mach and Reynolds numbers.) The aerodynamic pressure is in turn applied to the CTEF NASTRAN model, and CTEF deformation under both MFC actuation and aerodynamic loading is calculated. This procedure is iterated until a convergence is achieved. The convergence criterion is that the difference of CTEF deflections between iterations approaches zero. To avoid nonphysical, numerical divergence, a numerical damping technique is used: the aerodynamic force applied is an average of previous and current iterations. When convergence is achieved, the difference in the aerodynamic loads between iterations is also approaching zero. Thus it is a true convergence of the FSI procedure, that is the actual aerodynamic pressure loads generated by the current CTEF deflection are applied to the structure at convergence. The aerodynamic pressure is calculated on the CFD or XFOIL grid, which is normally different than the NASTRAN grid. Linear interpolation is used to map the aerodynamic loads from the fluid grids to the structure grids. In addition, when OVERTURNS is used for calculating the aerodynamic loads, the FSI solution using XFOIL is obtained first and used to set the CTEF deformation close to the final solution, so that fewer OVERTURNS iterations are needed. Although the sub-scale model is designed for testing in a heavy gas medium, air properties at standard sea level are used for simplicity in this study (Froude-scaled model.)

Analytical Results

The analytical results include the 2D structural predictions of CTEF deformation using NASTRAN and UM/VABS, 2D aerodynamic evaluations of CTEF airfoil by comparing OVERTURNS predicted aerodynamic coefficients and pressure distribution with those of the conventional DTEF, and 2D fluid and structure interaction simulations of CTEF deflection under aerodynamic pressure.

Structure Analysis

Figure 4 compares the NASTRAN and UM/VABS predictions of the CTEF deformations. The bimorph bender contains six layers of MFC-PZT plies with a thickness of 0.3mm for each layer. The airfoil deformations predicted by NASTRAN and UM/VABS show good agreement. The CTEF deflection angle, which is defined as rotation of the trailing edge (calculated as the rotation angle of a segment formed by the trailing-edge node and its adjacent node on the upper surface), is about two degrees with the MFC-PZT bimorph bender in the absence of aerodynamic loads.

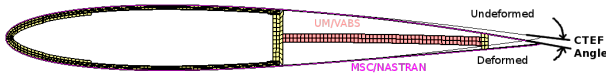
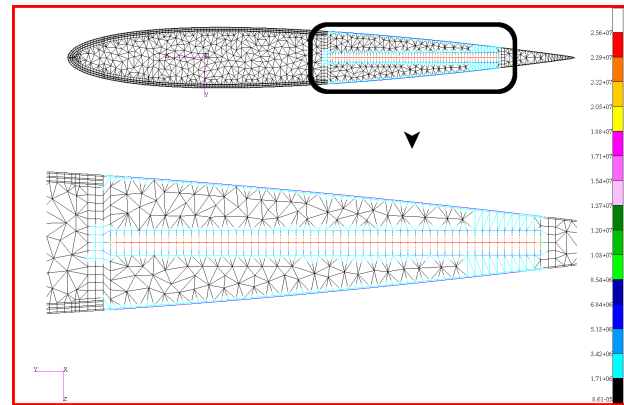


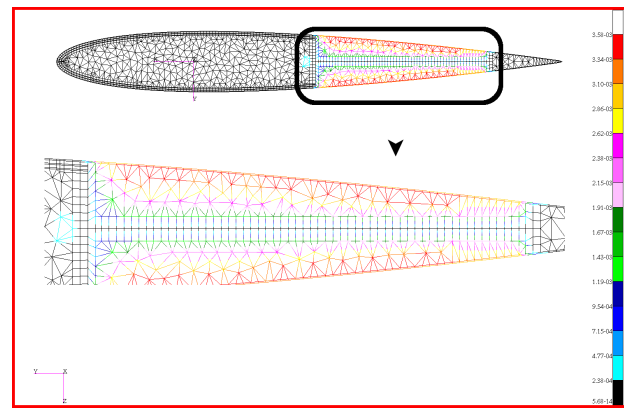
Figure 4: Comparison of NASTRAN and UM/VABS predicted CTEF deformation under MFC-PZT bimorph bender actuation (core material is removed from figure for clarity.)

The stress and strain distribution of CTEF under MFC-PZT actuation is presented in Fig. 5. Due to the symmetry of the NACA 0012 airfoil and symmetric layout of the cross-section including the MFC bimorph layers, the stress and strain distribution (von Mises) are also symmetric between upper and bottom portion of the CTEF cross-section. The mid plane of the MFC bender has virtually zero strain, but is the location of the maximum stress. This is because of the well-known block force and free strain relationship of piezoelectric materials. Away from the mid plane of the bender, a decrease in stress is observed along with a corresponding increase in strain. The stress level on the top and bottom surface of the bender approaches zero, whereas their strain approaches the free strain. The addition of more MFC layers will not further increase the CTEF deflection (as shown in Fig. 13,) because the required active strain is beyond the free strain (maximum active piezoelectric strain.) The core material has very little stress but large strain as they are flexible in the “Y” direction (bending stress/strain.) The skin layer has also light stress but large strain as it is also chosen to be soft to allow CTEF deformation. Front and rear ribs

exhibit small stress and strain levels, while the rest of the cross-section displays zero stress and strain. The airfoil elastic deformation occurs only at the portion where the MFC bender extends.



(a) Stress



(b) Strain

Figure 5: Stress and strain distribution of CTEF with 3+3 MFC-PZT layer bender.

A comparison of the CTEF deflection angles predicted by NASTRAN and UM/VABS for a range of voltages is presented in Fig. 6. Good agreement is observed between the analyses except that the NASTRAN predictions are slightly larger than those of UM/VABS. The difference in CTEF angle predictions between the analyses increases with the voltage, though it is small in magnitude. The CTEF angles predicted by NASTRAN increase linearly with voltage whereas those calculated by UM/VABS show some scattering.

Aerodynamics

The flow field of a deformed CTEF airfoil is examined in Fig. 7, which displays the OVERTURNS calculated density contour. The flow field of a deformed CTEF is similar to that of a DTEF. The deformed CTEF forces the air flows off the airfoil parallel to the deformed trailing

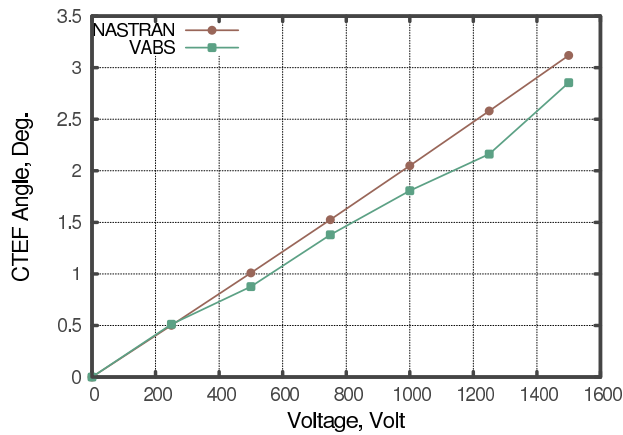


Figure 6: CTEF deflection angle vs. voltage with MFC-PZT bender.

edge, and changes the airfoil circulation in a manner similar to a deflected DTEF. Although the MFC bender starts at $0.50c$, the major CTEF deformation occurs rather close to the trailing edge. As such, the CTEF is not equivalent to a $0.50c$ DTEF. Instead, it matches a DTEF with a much smaller chord as shown in Fig. 8.

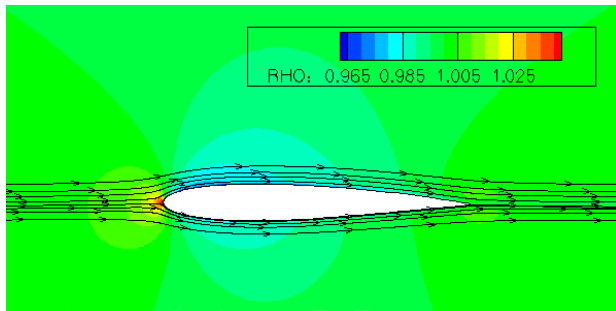


Figure 7: 2D OVERTURNS density contour of a NACA 0012 CTEF airfoil; AOA = 0° , Mach = 0.3, deformed CTEF angle = 2° .

The aerodynamic characteristics of a deformed CTEF and a deflected DTEF are compared in Fig. 8. The CTEF and DTEF are deflected with the same amount of angle: two degrees. The CTEF length is $0.50c$ (MFC bender starts at half chord) while DTEF has several flap chord sizes ranging from $0.15c$ to $0.50c$. The angle of attack is increased from 0 degrees to 8 degrees in two-degree increments. The variation of moment coefficients with lift coefficients predicted by OVERTURNS is displayed. It is shown that the $0.50c$ CTEF curve is between the curves of the $0.15c$ and $0.20c$ DTEF for all the angles of attack shown. This indicates that the aerodynamic characteristics of the CTEF are equivalent to those of a DTEF with flap size between $0.15c$ and $0.20c$. A DTEF with small flap chord has been shown to be preferable in the rotorcraft

vibration control application (Ref. 9).

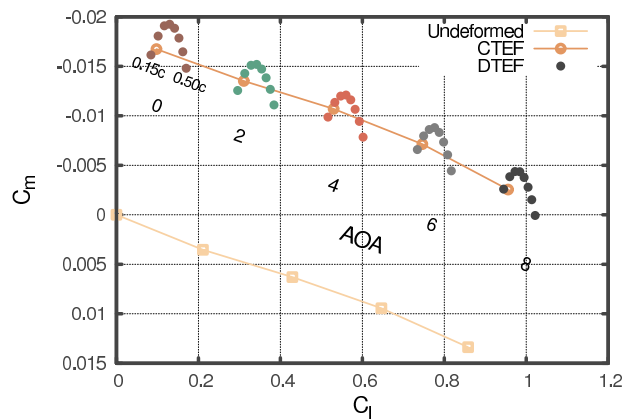
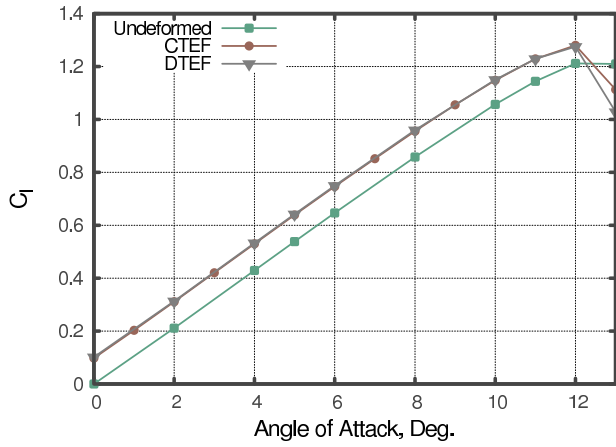


Figure 8: Comparison of CTEF and DTEF with different flap chord sizes; Mach = 0.3, CTEF and DTEF angles = 2° .

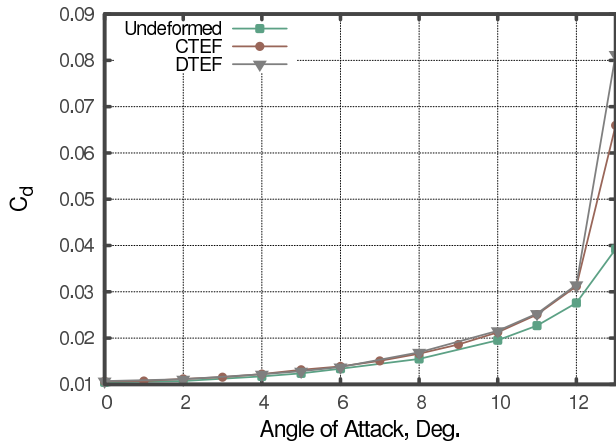
The aerodynamic coefficients of the $0.50c$ CTEF and $0.20c$ DTEF with two degrees of deflection are compared in Fig. 9. (The aerodynamic coefficients of an undeformed NACA 0012 are also shown for reference.) The $0.50c$ CTEF shows virtually the same variations of lift and drag coefficients with the angle of attack as those of the $0.20c$ DTEF. The magnitude of CTEF pitching moments is slightly less than that of the DTEF for all the angles of attack shown. In addition, the CTEF and DTEF airfoils have the same 12 degree stall angle although the CTEF airfoil shows a milder stall than the DTEF airfoil.

Figure 10 further compares the deformed CTEF and DTEF by comparing the predicted pressure distribution of the deformed CTEF and DTEF airfoils at two angles of attack. The OVERTURNS predicted pressure distributions of the $0.50c$ CTEF and $0.20c$ DTEF are very similar at both angles of attack: 0 and 8 degrees. There are small deviations, however, where the flap deflections begin: $0.50c$ for the CTEF and $0.80c$ for the DTEF. The similarity between the aerodynamic characteristics of CTEF and DTEF with the same deformation angle indicates that the CTEF angle, which is defined as the rotation angle of the trailing edge, is a meaningful measurement of the CTEF aerodynamic effectiveness.

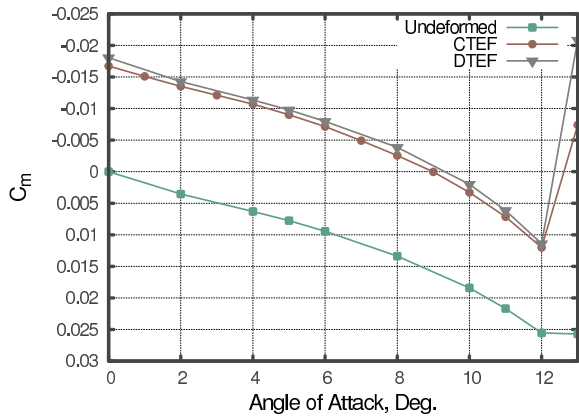
In order to examine whether the aerodynamic pressures predicted by XFOIL have sufficient accuracy, they are compared with OVERTURNS predictions at two angles of attack (Fig. 11.) Good agreement is observed between the two analyses, except that the XFOIL pressure distribution is slightly larger in magnitude, especially at the larger angle of attack. The differences between the analyses are small, however, and XFOIL provides sufficient accuracy to supplement OVERTURNS where high computation efficiency is required, such as in design optimization using



(a) Lift coefficient



(b) Drag coefficient



(c) Pitching moment coefficient

Figure 9: Comparison of aerodynamic coefficients of the 0.50c CTEF and 0.20c DTEF; Mach = 0.3, CTEF and DTEF angles = 2°.

the fluid and structure interaction procedure.

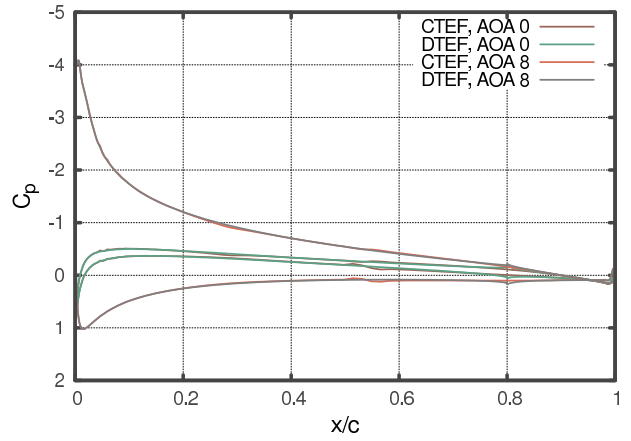


Figure 10: Comparison of pressure distribution of the 0.50c CTEF and 0.20c DTEF.

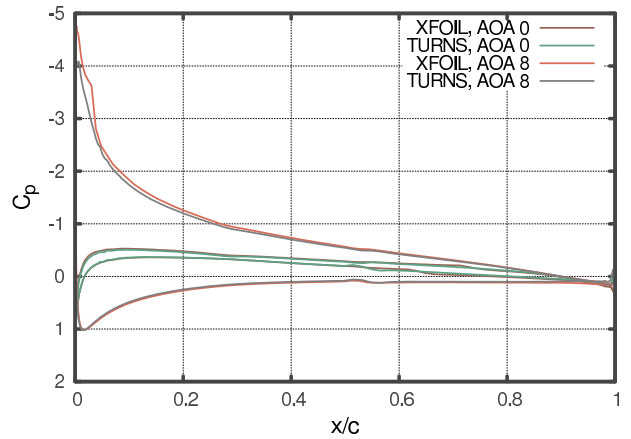


Figure 11: Comparison between pressure distributions predicted by XFOIL and OVERTURNS.

2D Static Coupling of Structure and Aerodynamics

The convergence history of the fluid structure interaction procedure is illustrated in Fig. 12. The uncoupled (structure analysis only; no aerodynamic force) CTEF angle is about two degrees. The CTEF deflections under aerodynamic pressure are calculated at several angles of attack ranging from 0 to 6 degrees. The FSI procedure begins with the coupling of NASTRAN and XFOIL. Once FSI with XFOIL converges, OVERTURNS calculated pressure loads are applied, and the coupled NASTRAN-OVERTURNS procedure is executed until convergence. The convergence with XFOIL pressure is achieved at iteration step No. 3 for all the AOA cases, except AOA of four which is converged at step No. 4. For an AOA of 0 degrees, the FSI with OVERTURNS converges in one step at iteration No. 4, because the aerodynamic pressures predicted by XFOIL and OVERTURNS are very close.

(For illustration purposes, all the converged solutions are extended to iteration No. 7.) For the other AOAs, the convergences with OVERTURNS take three iterations. The CTEF deflections show larger reductions with higher angles of attack. This is because the differential pressure on top and bottom airfoil surfaces increases with angles of attack, similar to the hinge moment of a DTEF (Ref. 21). This variation of differential pressure with angle of attack is correctly predicted by OVERTURNS. The reduction in magnitude is small, however, the largest reduction with OVERTURNS is 2.6% at AOA of 6 degrees.

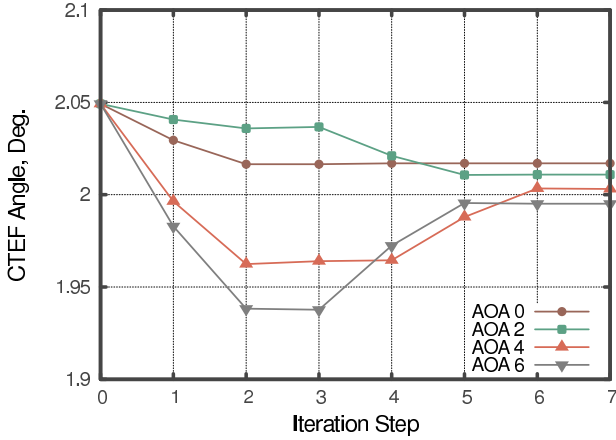


Figure 12: FSI convergence history.

The FSI procedure is then used to examine the effect of numbers of MFC layer on CTEF angle with aerodynamic pressure applied (Fig. 13.) In order to fit maximum seven MFC layers inside the airfoil profile, the MFC bender length is reduced from the baseline 0.40c to 0.35c by moving the aft rib 0.05c forward. This reduction in bender length results in a reduction of the uncoupled CTEF angle from the baseline value of 2 degrees to 1.7 degrees. Figure 13(a) illustrates that the CTEF angle reaches the maxima with three layers of MFC-PZT layers (three on top and three on bottom of the bender) for both the uncoupled and FSI coupled cases. The reason is explained in Fig. 5: strain on the outer layers approaches the free strain of MFC, and further increasing the number of layers will add stiffness but not actuation force. A similar trend is shown for the MFC-PMN bender (Fig. 13(b).) The maximum uncoupled CTEF deflection with MFC-PMN is approximately the same as that of MFC-PZT. The reason is that the MFC-PMN has higher active strain than that of MFC-PZT but lower longitudinal stiffness (Ref. 20), and these two effects cancel each other with regards to generating CTEF deformation. The maximum CTEF deflection is achieved with four layers of MFC-PMN instead of three with MFC-PZT, and also larger reductions are shown when the aerodynamic pressure is applied.

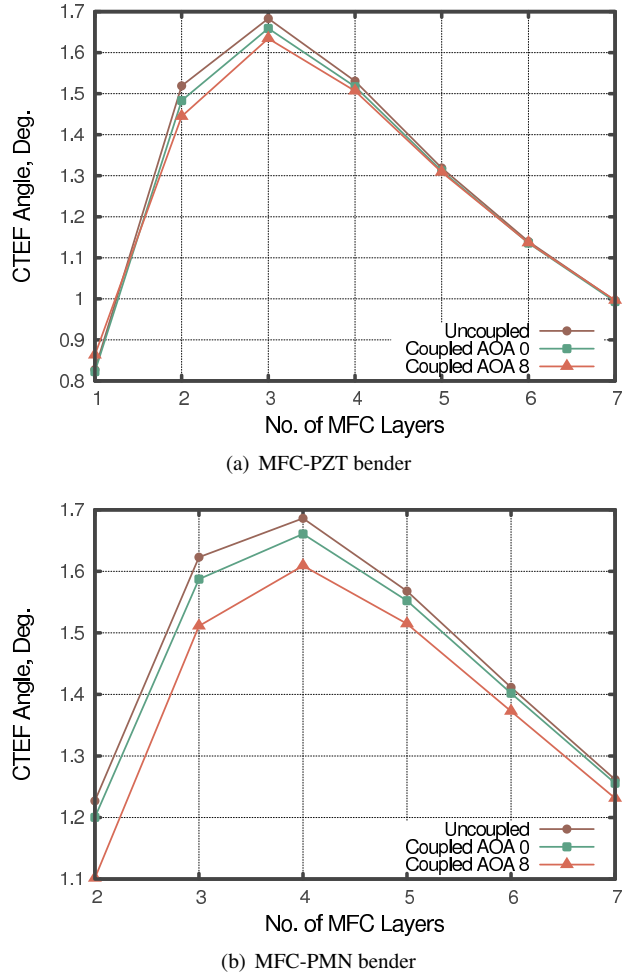


Figure 13: Variation of CTEF deflection with number of MFC layers.

It is possible to achieve larger CTEF deflection by mixing MFC-PZT and MFC-PMN layers in the bender than obtained by using the materials alone. An example of this is presented in Fig. 14, which compares the maximum CTEF deflection angles with different MFC bender constituents: three layers of MFC-PZT only, four layers of MFC-PMN only, and two layers of MFC-PZT and one layer of MFC-PMN on the outside. It is shown that the mixing MFC-PZT/MFC-PMN bender has the maximum CTEF deflections for both the uncoupled and coupled cases. A mixed MFC-PZT and MFC-PMN bender generates 8% more CTEF deflection than an MFC-PZT or an MFC-PMN only bender for the coupled case. The MFC-PZT is more effective than the MFC-PMN as the inside layers of the bender, where strain is small, because its high stiffness generates more actuation force. MFC-PMN is more effective than MFC-PZT as the outside layer, where required strain is large, since the smaller active strain of MFC-PZT limits its actuation authority.

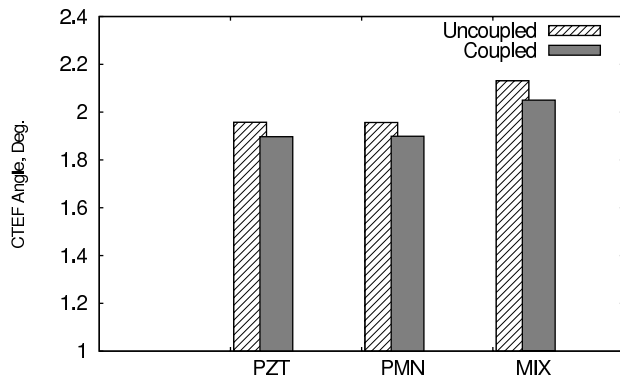


Figure 14: Comparison of CTEF deflections with different MFC constituents.

Summary and Conclusions

The preliminary design and evaluation of an airfoil with active continuous trailing-edge flap (CTEF) has been presented as a potential rotorcraft active control device. The development of structural cross-section models of a continuous trailing-edge flap airfoil was described. The CTEF deformations with MFC actuation are predicted by NASTRAN and UM/VABS, and showed good agreement. The 2D aerodynamic characteristics of the continuous trailing-edge flap were evaluated using the CFD analysis OVERTURNS. The comparison of the aerodynamic efficiency of a continuous trailing-edge flap to a conventional discrete trailing-edge flap was also performed. A fluid structure interaction procedure was implemented, and used for predicting deflection of the continuous trailing-edge flap under aerodynamic pressure. The following concluding remarks were offered, subject to the limitations of the analysis and the scope of this study:

1. A MFC bender of relatively small numbers of layer achieves maximum CTEF deflection for the sub-scale model: six layers of MFC-PZT (three on top and three on bottom) obtains two degrees of CTEF deformation.
2. The aerodynamic characteristics of CTEF and DTEF are similar for the same displacement angle, where the CTEF angle is defined as the rotation angle of the trailing edge.
3. The equivalence of CTEF and DTEF is for different flap chord sizes: the aerodynamic characteristics of a 0.50c CTEF is comparable to a DTEF with a flap chord size between 0.15c and 0.20c with the same deflection angle.
4. The reductions in CTEF deflection are relatively small when the aerodynamic pressure is applied: 2.6% reduction is shown with a CTEF deflection

angle of two degrees and at an angle of attack of six degrees.

5. Newly developed MFC-PMN supplements MFC-PZT when applied as outsider bender layers. A mixed MFC-PZT and MFC-PMN bender generates 8% more CTEF deflection than an MFC-PZT or an MFC-PMN only bender under aerodynamic loads.

Acknowledgements

The authors gratefully acknowledge Prof. Carlos Cesnik and his research group at the University of Michigan for assistance on running UM/VABS analysis, and Prof. James Baeder and his group at the University of Maryland on using 2D OVERTURNS.

References

- ¹Ellis, C. W. and Jones, R., "Application of an Absorber to Reduce Helicopter Vibration Levels," *Journal of the American Helicopter Society*, Vol. 8, (3), July 1963, pp. 30–42.
- ²Welsh, W., Fredrickson, C., Rauch, C., and Lyndon, I., "Flight Test of an Active Vibration Control System on the UH-60 Black Hawk Helicopter," American Helicopter Society 51st Annual Forum Proceedings, Fort Worth, TX, May 9-11 1995.
- ³Chopra, I., "Status of Application of Smart Structures Technology to Rotorcraft Systems," *Journal of the American Helicopter Society*, Vol. 45, (4), October 2000, pp. 228–252.
- ⁴Gagliardi, A., *CFD Analysis and Design of a Low-Twist, Hovering Rotor Equipped with Trailing-Edge Flaps*, Ph.D. thesis, Department of Aerospace Engineering, University of Glasgow, August 2007.
- ⁵Thornburgh, R. P., Kreshock, A. R., and Wilbur, M. L., "Structural Optimization of Active-Twist Rotor Blades," American Helicopter Society 67th Annual Forum Proceedings, Virginia Beach, VA, May 3-5 2011.
- ⁶Wilbur, M. L., Mirick, P. H., William T. Yeager, J., Langston, C. W., Cesnik, C. E. S., and Shin, S., "Vibratory Loads Reduction Testing of the NASA/Army/MIT Active Twist Rotor," American Helicopter Society 57th Annual Forum Proceedings, Washington, D.C., May 9-11 2001, p. 19.
- ⁷Maucher, C. K., Grohmann, B. A., Janker, P., Altmikus, A., Jensen, F., and Baier, H., "Actuator Design for the Active Trailing Edge of a Helicopter Rotor Blade," *Innovation*, 2007, pp. 12.

⁸Grohmann, B., Muller, F., Achci, E., Pfaller, R., Bauer, M., Maucher, C., Dieterich, O., Storm, S., and Janker, P., "Design, Evaluation and Test of Active Trailing Edge," American Helicopter Society 67th Annual Forum Proceedings, Virginia Beach, VA, May 3-5 2011.

⁹Shen, J., Yang, M., and Chopra, I., "Swashplateless Helicopter Rotor System with Trailing-Edge Flaps for Flight and Vibration Controls," *Journal of Aircraft*, Vol. 43, (2), April-May 2006, pp. 346–352.

¹⁰Fogarty, D. E., Wilbur, M. L., and Sekula, M. K., "The effect of Non-Harmonic Active Twist Actuation on BVI Noise," American Helicopter Society 67th Annual Forum Proceedings, Virginia Beach, VA, May 3-5 2011.

¹¹Norman, T. R., Shinoda, P. M., Kitaplioglu, C., Jacklin, S. A., and Sheikman, A., "Low-Speed Wind Tunnel Investigation of a Full-scale UH-60 Rotor System," American Helicopter Society 58th Annual Forum Proceedings, Montreal, Canada, June 11-13 2002, p. 20.

¹²Cole, S. R. and Rivera, Jr., J. A., "The New Heavy Gas Testing Capability in the NASA Langley Transonic Dynamics Tunnel," Royal Aeronautical Society Wind Tunnels and Wind Tunnel Test Techniques Forum, Churchill College, Cambridge, UK, April 14-16 1997.

¹³*NASTRAN Quick Reference Guide*, The MacNeal Schwendler Corporation.

¹⁴Palacios, R. and Cesnik, C., "Cross-Sectional Analysis of Nonhomogeneous Anisotropic Active Slender Structures," *AIAA Journal*, Vol. 43, (12), 2005, pp. 2624–2638.

¹⁵Jose, A. I., Sitaraman, J., and Baeder, J. D., "An Investigation into the Aerodynamics of Trailing Edge Flap and Flap-Tab Airfoils Using CFD and Analytical Methods," American Helicopter Society 63rd Annual Forum Proceedings, Virginia Beach, VA, May 1-3 2007, p. 21.

¹⁶Drela, M., "XFOIL: An Analysis and Design System for Low Reynolds Number Airfoils," Conference on Low Reynolds Number Airfoil Aerodynamics, University of Notre Dame, June 1989.

¹⁷*Patran User's Manual*, The MacNeal Schwendler Corporation.

¹⁸Reaves, M. C. and Horta, L. G., "Piezoelectric Actuator Modeling Using MSC/NASTRAN and MATLAB," Technical Report NASA/TM-2003-212651, Langley Research Center, Hampton, Virginia, October 2003.

¹⁹Ivan, I. A., Rakotondrabe, M., Agnus, J., Bourquin, R., Chaillet, N., Lutz, P., Poncot, J.-C., Duffait, R., and Bauer, O., "Comparative Material Study between PZT Ceramic

and Newer Crystalline PMN-PT and PZN-PT Materials for Composite Bimorph Actuators," *Reviews on Advanced Materials Science*, Vol. 24, (1), 2010, pp. 1–9.

²⁰Wilkie, W. K., Inman, D. J., Lloyd, J. M., and High, J. W., "Anisotropic Laminar Piezocomposite Actuator Incorporating Machined PMN-PT Single Crystal Fibers," *Journal of Intelligent Material Systems and Structures*, Vol. 17, (1), 2008, pp. 15–28.

²¹Abbott, I. H. and Doenhoff, A. E. V., *Theory of Wing Sections*, Chap. High-Lift Devices, Dover Publications, Inc., 1959.